A Physical Model for Understanding the Activation of MoS_2 Basal-plane Sulfur Atoms for the Hydrogen Evolution Reaction

Mingjie Liu, Mark S. Hybertsen, and Qin Wu*

[*] Dr. M. Liu, Dr. M. S. Hybertsen, Dr. Q. Wu
Center for Functional Nanomaterials, Brookhaven National Laboratory
Upton, NY 11973 (USA)
E-mail: qinwu@bnl.gov

Supporting information for this article is given at the end of the document.

Abstract: *Weak binding of hydrogen atoms to the 2H-MoS_2 basal plane renders MoS_2 inert as an electrocatalyst for the hydrogen evolution reaction. Transition metal doping can activate neighboring sulfur atoms in the MoS_2 basal plane to bind hydrogen more strongly. Our density functional theory-based studies show strong variation in the degree of activation by dopants across the 3d transition metal series (Ti, V, Cr, Mn, Fe, Co, Ni, Cu and Zn). To understand the trends in activation, we propose a theoretical model based on the electronic promotion energy required to convert the full valence shell of a local sulfur atom to be partially open and therefore ready to bond with a hydrogen atom. In general, the promotion is achieved through an electron transfer from the sulfur to neighboring metal atom sites. Furthermore, we demonstrate a specific, electronic-structure based descriptor for hydrogen binding strength: Δ_{dp}, the local interband energy separation between the lowest empty d-states on the dopant metal atoms and occupied p-states on S. This model can be used to provide guidelines for chalcogen activation in future catalyst design based on doped transition metal dichalcogenides.*

Introduction

Earth-abundant transition metal dichalcogenides (TMDs) have emerged as strong candidates for electrocatalysis because of their favorable electrochemical properties.[1] In particular, MoS_2 based electrocatalysts have been studied for many reactions such as the hydrogen evolution reaction (HER),[2] the CO_2 reduction reaction,[3] the oxygen reduction reaction[4] and the nitrogen reduction reaction.[5] Take HER for example, an essential reaction in water splitting that produces hydrogen as the energy carrier. Tremendous effort has been made to adapt MoS_2 based materials as electrocatalysts. The goal is to replace Pt due to its high cost, although presently Pt is the most efficient HER electrocatalyst [2c, 6]. The overall catalyst activity depends critically on the total number of active sites. On metal surfaces, including those on nanoparticles, steps, kinks and corners can all serve as active sites.[7] For pure MoS_2, however, active sites have been shown to be largely limited to the edges of terraces or islands.[7,8] As a result, most research directed to MoS_2 catalysts has focused on increasing the density of edges through ingenious, but difficult, nanostructure engineering.[9],[10] An alternative approach to increasing active sites in MoS_2 is through activation of basal-plane sulfur atoms, such as, by transition metal (TM) doping. This has potential to be a more easily controlled process than edge engineering.[11] Previous work on doping-enabled MoS_2 catalysts have reported several effective metal dopants; Ni,[12] Pt,[13] Zn,[14] Pd[15] and Co[16] were all shown to boost the HER activity on the MoS_2 basal plane. However, a general understanding of the mechanism is still lacking. A theoretical model that can predict the HER activity for TM-doped MoS_2 surfaces can have significant impact for the design of future catalysts.

A complete account of HER activity requires consideration of many factors, including solvation, electrolytes, kinetics and dynamics. However, it is also known that the Gibbs free energy of hydrogen adsorption (ΔG_H) can be used to predict the trends in HER catalyst performance, for both homogeneous and heterogeneous catalysts.[2c, 17] In particular, catalysts with optimal HER activity have been shown to correspond to near-zero hydrogen adsorption free energy.[18] Trends in ΔG_H are dominated by the binding energy of hydrogen atoms to the catalysts. Fundamentally, the binding energy can be related to the intrinsic electronic structure of the catalyst. For screening purposes, there is a significant advantage to identifying descriptors based on intrinsic catalyst electronic structure, without further reference to more complex reaction processes.[18-19] For example, the *d* band center in transition metal-based catalysts[20] has been successfully applied in many cases.[21]

In contrast, the binding of H atoms with the basal-plane S atoms of TM-doped MoS_2 is not well understood. It is unclear what physical descriptor determines whether specific choices of TM doping will activate nearby inert basal-plane sulfur atoms for the HER. Several intrinsic descriptors have been proposed for MoS_2 and other TMD materials. These include the lowest unoccupied state energy relative to the vacuum level,[22] the local Bader charges,[16a] antibonding electron transfer,[23] and band centers.[24] However, as we will show in detail in a later section, these models all have a limited scope of application. A comprehensive understanding of the sulfur activation towards H binding is still needed.

We address this challenge by proposing a theoretical model for the activation of basal-plane sulfur atoms for HER activity in MoS_2. Unlike surface atoms in transition metals, oxides or other bulk materials, S atoms in the basal plane of MoS_2 and other 2D materials are not under-coordinated. In either the covalent or the ionic bonding model for these compounds, the S atoms have a nominally full valence shell. This is the natural explanation for their relative inertness. It also suggests that a key factor in the activation of a local S atom in the basal plane is to bring it into an electronic state with the valence shell partially open. Then the subsequent formation of a bond with a hydrogen atom should be energetically favorable. We propose a H-S binding model that is based on this hypothetical two-step process: an endothermic electronic promotion process to bring a S site into a pre-bonding state followed by exothermic H-S bonding formation. (Figure 1) Based on this model, we can understand the trends in H-S binding strengths and predict them with a quantitative descriptor, Δ_{dp}, the

interband distance between the empty *d* orbital in Mo (or metal dopants) and occupied *p* orbital in S. We use density functional theory (DFT) based calculations[25],[26],[27],[28] (see details in SI) to explore the degree of S activation for hydrogen binding across nearly 30 different 3*d* metal doped MoS_2 systems. The binding of hydrogen to local S sites varies considerably with dopant choice and local dopant complex formation. Using the computed results, we demonstrate that our proposed descriptor, Δ_{dp}, is quantitatively effective in predicting the hydrogen binding energy.

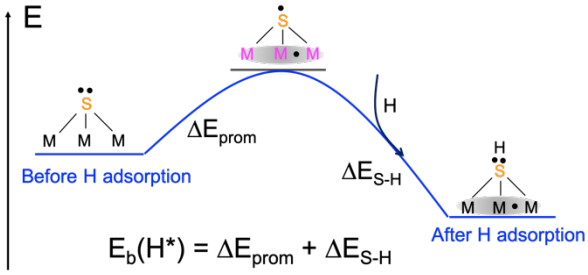

Figure 1. Physical model for H-S bond formation: (1) an electronic promotion process that pushes an electron from the full valence shell of S to neighboring metal atoms; (2) H binding to fill the partially open valence shell of the S site.

In the following, we will first determine the most stable structures with different dopant concentrations by enumerating possible dopant configurations. We will explain local distortions caused by the dopant atoms and how sulfur vacancy formation becomes favorable in some situations. We find that the dopants tend to form local complexes in which they replace the Mo atoms connected to the same sulfur. This sulfur atom becomes the most active site for hydrogen binding. We next present our model and show how the hydrogen-binding energy correlates with the descriptor we constructed, the interband energy separation Δ_{dp}. This is followed by a detailed comparison with other existing descriptors, where we explain why our model has the broadest applicability. Finally, we will discuss the limitations and possible future improvements of the current model.

Results and Discussion

Dopant Structures and the H Adsorption Sites

We build models with metal dopants substituting for selected Mo atoms in the MoS_2 layer, following previous studies [13, 29]. To account for different dopant concentrations, we have considered a single dopant (1M), two dopants (2M) and three dopants (3M) in a (4x4) MoS_2 supercell, corresponding to doping concentrations of 6.25%, 12.5% and 18.75%, respectively.

For a single dopant, the local structures for Fe, Co, Ni and Cu experience a lattice distortion where the C_{3v} symmetry is broken (Figure S1). This is consistent with previous reports of lattice distortion observed in DFT-based studies for these dopants[30] and specifically for for Ni-doped MoS_2 in experiments.[12a] The energy difference between the high- and low-symmetry structures is shown in Figure 2a. The low-symmetry structure has unequal M-S bond lengths with $l_3>l_1=l_2$ as shown in the inset of Fig 2a. Details of the M-S bond lengths can be found in Table S1. Based on the lowest-energy H-adsorption configuration, the H atom tends to bind to the sulfur next to the dopant atoms. In the case of low symmetry configurations, where there are two different S atoms next to the dopant atom, the H prefers to bond to the one S with the longer bond to the metal atom, i.e., l_3 in Figure 2a.

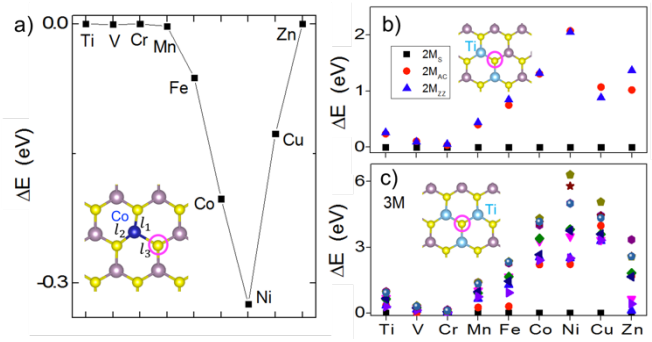

Figure 2. a) Energy difference between low- and high-symmetry structures for 1M-doped MoS_2. b), c) Energy of different 2M-doped (b) and 3M-doped (c) MoS_2 configurations relative to the lowest energy configuration for each dopant. For 1M, 2M and 3M, an example of the stable configuration is shown in the inset with the strongest H-binding S site circled.

For a given doping concentration, the metal dopants prefer to substitute for Mo sites that bond to common sulfurs, forming local complexes. With two metal atoms substituting Mo, within the (4x4) supercell model used here, there are three possible configurations for 2M (Figure S2): two dopants share the same S ($2M_S$); two M in the armchair direction ($2M_{AC}$); and two M in the zigzag direction with one Mo in between ($2M_{ZZ}$). We found that the $2M_S$ configurations are the lowest energy one for all the dopants (Figure 2b). For systems with 3 dopant atoms (3M), we enumerate all possible configurations by considering the transitional and rotational symmetry and identify eleven cases (Figure S4). Similar to the 2M cases, the most stable configuration is the one with three M sharing the same sulfur site (Figure 2c). However, for late transition metals, both $2M_S$ and $3M_S$ configurations experience significant local distortion (Figures S3 and S5). Particularly, in the 3Ni and 3Cu cases, one of the two sulfurs coordinating the three dopant atoms is pushed out of plane. This signals an instability in the defect complex to formation of a sulfur vacancy (Vs).

Indeed, for late transition metals, the high doping concentration destabilizes the sulfur site that connects to multiple dopant atoms. Sulfur vacancy formation is preferable. The local complex then consists of two or three dopant atoms on Mo sites adjacent to one S atom and a V_S. Physically, the small dopant atom size in these cases forces both sulfur atoms in the same site to move towards the middle plane, but the S-S repulsion pushes one of them out. This leads to a sulfur vacancy at that site. This instability for the late transition metal dopants in 2M and 3M cases is characterized by calculating the sulfur vacancy (Vs) formation energy. As shown in Figure 3a, for 3Fe, (2, 3)Co, (2, 3)Ni, (2, 3)Cu and (2, 3)Zn, the Vs formation energy is negative, indicating that these dopant complexes are not stable against the formation of a sulfur vacancy. After forming a vacancy, the remaining sulfur atom sits at the Mo middle plane (Figure 3b). That S site is also the preferred location for H binding in these complexes. For all doped structures with negative E_f(Vs) we will use the structure with S vacancy in the analysis of H adsorption. Because 3Mn has a very small positive E_f(Vs), we include both structures, with and without S vacancy.

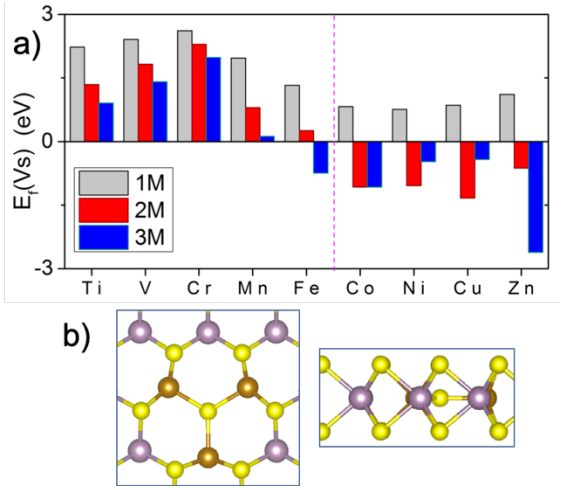

Figure 3. a) Sulfur vacancy formation energy for 1M, 2M and 3M doped MoS_2 systems. b) Top and side view of the defect complex 3Fe-Vs, representative of the results for late transition metal dopants.

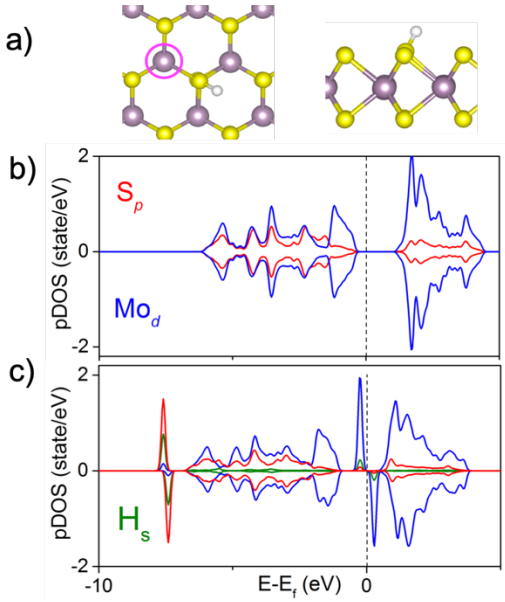

Figure 4. a) Top and side views of H-S binding configuration. b) The PDOS on S and Mo in pristine MoS_2. c) The PDOS of local S, Mo and H after H adsorption.

Electronic Structure Model for S Activation and H-S Binding

To introduce our physical model for understanding the H-S binding strength, we start with an analysis of the electronic structure features associated with H-S bond formation on pristine MoS_2. Figure 4a shows the most stable configuration for H adsorption on pristine MoS_2, where the S-H bond is slightly tilted towards the center of the hexagon. There is also a stable configuration with H vertically on top of the S but it is 0.28 eV higher in energy. Figure 4b shows the projected density of states (PDOS) on sulfur *p* and Mo *d* states for pristine MoS_2. The PDOS for the proximal Mo and S sites and the H atom upon H-adsorption are shown in Figure 4c. The sulfur that binds to the H atom and the Mo (marked with purple circle in Figure 4a) that connects to this S are used in the projection.

As shown in Figure 4b, the pristine MoS_2 has a moderate band gap, which explains its stability. In terms of the local electronic structure, the sulfur is inert because its valence shell is full after nominally accepting two electrons from neighboring Mo atoms. Upon H adsorption (Figure 4c), the S atom, with its valence shell still full, clearly forms a single bond with the H atom, evidenced from the new narrow H-S band below the Mo-S band. At the same time, a local shallow electronic state is created on its neighboring Mo atoms and filled with one electron. This observation leads us to hypothesize the two-step H-S binding process introduced above in Figure 1. The first step is an electronic promotion process where an electron in the valence shell of the S atom is pushed back to Mo atoms, thus leaving S with an open valence shell. The valence shell of S will be filled again after it forms a single bond with the H atom in the second step. The extra electron remains localized on nearby Mo sites. Therefore, the H-S binding energy can be viewed as the sum of the energy cost to promote S into the state of open valence shell and the energy gain from H-S bond formation, i.e. $E_b = \Delta E_{prom} + \Delta E_{S\text{-}H}$ (Figure 1). This separation can help us understand the dopant effects on the H-S binding. It is plausible to hypothesize that $\Delta E_{S\text{-}H}$ is an intrinsic property of the active sulfur atom that depends weakly on the local environment. Then, the net effects due to the dopants can be ascribed mainly to changing ΔE_{prom}. Consequently, the trend in H-S binding strength can be revealed in the energy cost associated with the first, electronic promotion process.

To find out what determines the electronic promotion energy, we examine more closely the electron transfer from S to neighboring metal atoms. In the band picture, the minimum transfer energy involves an electron from sulfur *p*-states right below the Fermi level being pushed into metal atom *d*-states right above the Fermi level. However, the energy cost to create a hole in a local S atom *p*-shell is better represented by the centroid of the local *p*-band. This leads to the descriptor denoted as Δ_{dp}, representing the interband distance between occupied S *p*-states and unoccupied neighboring metal *d*-states illustrated in Fig. 5a. Quantitatively, we use the following formula to calculate Δ_{dp},

$$\Delta_{dp} = \varepsilon_d - \varepsilon_p = \frac{\int_{E_f}^{1e} \varepsilon\, n_d}{\int_{E_f}^{1e} n_d} - \frac{\int_{-\infty}^{E_f} \varepsilon\, n_p}{\int_{-\infty}^{E_f} n_p}. \quad (1)$$

The integration of the sulfur *p*-states is over the whole occupied *p* band up to the Fermi level. This *p* band center approximates the energy level of the S local *p* state. The integration of the *d*-states is over the unoccupied *d*-orbitals of all three metal atoms surrounding the sulfur atom, and the range is from the Fermi level to the point where the one extra electron is added to the supercell. The band center of this limited integration range represents the lowest unoccupied orbital level.

To examine the effectiveness of our electronic structure-based descriptor, we initially put aside the role of structural relaxation. Specifically, rigid structures from the final, relaxed H-adsorption structures are used. The hydrogen binding energy is determined as the H removal energy without further relaxation. The local

PDOS are calculated for the structure once the H atom is removed. The role of the local structural changes will be addressed later.

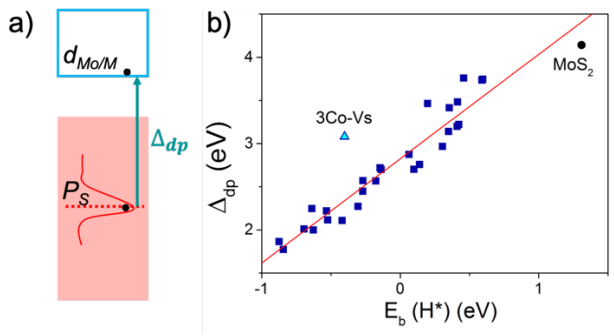

Figure 5. a) Electronic structure-based descriptor, Δ_{dp}, for the promotion process. b) Correlation between Δ_{dp} and the H binding energy (see Computational Methods in SI for the definition of E_b) for pure MoS_2 and the dopant complexes. Rigid structures from relaxed H-adsorption configurations are used. Red line: linear fit without the 3Co-Vs outlier (y=1.21x+2.82; R^2=0.92).

The correlation between Δ_{dp} and the hydrogen binding energy is shown in Figure 5b. Excluding 3Co-Vs, an outlier to be discussed below, the other data points can be well represented by a linear relationship. The positive slope manifests that smaller interband distance leads to stronger hydrogen binding, consistent with our qualitative understanding. The magnitude of the slope (1.21) is close to one, validating our hypothesis that the electronic promotion energy, captured in our descriptor Δ_{dp} is responsible for most of the variation in hydrogen binding energy across the different dopant complexes. Figure 5b is a remarkable result because there are different dopant elements, concentrations, and degrees of distortion from the underlying MoS_2 lattice; some dopant complexes even include S vacancies. In total, there are nearly 30 data points covering a range of over 2 eV in the binding energy, whose variation can now be understood with the descriptor.

Our model provides a physical explanation that accounts for different doping effects on MoS_2 reactivity. Figure 6 shows a few representative cases of the PDOS and the relationship to our descriptor Δ_{dp}. For the case of an isolated Cr dopant, a band gap is preserved in the local PDOS (Figure 6a), but it is reduced compared to the pure MoS_2 gap (Figure 4b). The smaller size of Cr leads to a weaker interaction with S. The smaller gap in the local PDOS directly results in smaller Δ_{dp}, 3.41 eV as compared to 4.14 eV for MoS_2. Correspondingly, locally H bonds more strongly to the adjacent sulfur in 1Cr-MoS_2 (E_b of 0.35 eV versus 1.31 eV). For transition metal dopants to the left of Cr in the 3*d* series, unoccupied *d* states are available at the top of the valence band because there are fewer *d* electrons. This is illustrated for the case of V doping (Figure 6b), and it results in a much reduced Δ_{dp} (2.87 eV) and enhanced E_b (0.06 eV). Dopants to the right of Cr generate gap states between the conduction band and valence band as illustrated for the case of Fe doping (Figure 6c). These localized gap states are partially occupied. Once again, there are unoccupied *d* levels available immediately above the Fermi level. As a result, 1Fe-MoS_2 has a smaller Δ_{dp} (2.57 eV) and a stronger H binding energy (-0.27 eV). For reference, a complete set of Δ_{dp} and E_b data can be found in Table S2.

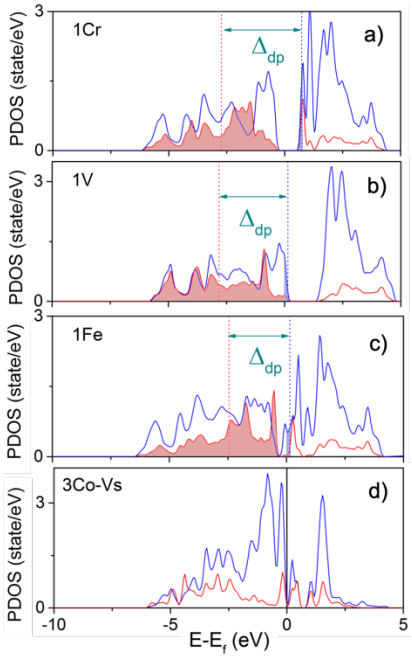

Figure 6. PDOS and Δ_{dp} for (a) 1Cr, (b) 1V, and (c) 1Fe doped MoS_2. The *p* and *d* integration areas are shaded in red and blue, respectively. Dotted vertical lines represent the locations of ε_p and ε_d. d) PDOS for the outlier case of 3Co doped MoS_2 with a sulfur vacancy.

Comparisons with Other Descriptors

Our model provides the most comprehensive understanding for the basal plane activation in TMD materials in comparison with several recent studies. Two previously suggested descriptors can be viewed as special cases of our model. Ouyang et al.[24] have considered different classes of defects in MoS_2. For those defects where H adsorbs through formation of a S-H bond, they use ε_p as the descriptor. According to our model, this will work well if there are *d* states immediately above the Fermi level, i.e. $\varepsilon_d \approx 0$. However, if there is a significant band gap, ε_p alone will not work. A plot of ε_p against E_b(H*) using our data (Figure S6) supports this picture. In separate work, Liu et al.[22] suggested the lowest unoccupied state (LUS) level is a descriptor for covering the scope of MX_2 substrates without defects. Recognizing that the empty band in all of these materials is predominately due to metal *d*-states, their descriptor is equivalent to ε_d in our model. While this works for pristine materials, it would be less useful for understanding the effects of dopants and defects. With considerations of the local *p* level, our Δ_{dp} model is therefore more general.

Deng et al.[16a] considered a series of 10 transition metal dopants in the 1M doped configuration and proposed the Bader charge of the S atom as a descriptor. Since the local charge on S atom affects its local *p* energy level, there is a connection to the Δ_{dp} descriptor. However, considering the full scope of the dopant-based defect complexes studied here, our results (Figure S7) show that the correlation between Bader charge and the H binding energy is much lower than what we find for our descriptor that directly measures the electron promotion energy. Very recently, Yu et al.[23] presented a general model that emphasizes antibonding electron transfer. Their picture can be understood from the inverse of the two-step process in Figure 1. The full valence S atom interacts with a H atom leading to occupation of an antibonding orbital from the S-H interaction. Subsequent

electron transfer to the Fermi level lowers the energy. While the physical picture is similar, it is less useful as a descriptor since the antibonding orbital level is only known with a post-adsorption bonding analysis. This limits its use as a method for materials prescreening.

Limitations of the Model

Our model provides a physical understanding of the key elements in the sulfur activation process. In particular, the degree of activation is understood from the local electronic structure changes and their relationship to the energy cost to open the nominally filled S *p*-shell. However, in rare cases, the local S atom in the defect complex already has a partially open *p*-shell and our descriptor is not as quantitatively predictive. This is the case for 3Co-Vs, the outlier in Figure 5b. The fit line to the descriptor Δ_{dp} data would suggest weaker E_b(H*) than what is found in the DFT calculations. The PDOS for the active S and the average of the three dopants plotted in Figure 6d shows substantial local sulfur *p* state density straddling the Fermi level. At the same time, there is a magnetic moment of 0.2μ_B on the S atom. These electronic features indicate that the S atom valence shell is not full. In the framework of our model, it can be understood that Δ_{dp} overestimates the promotion energy required to bring this sulfur atom into the state for the S-H bond formation. Interestingly, the 3Co-Vs case is found to be a good HER catalyst in a recent experimental study.[31]

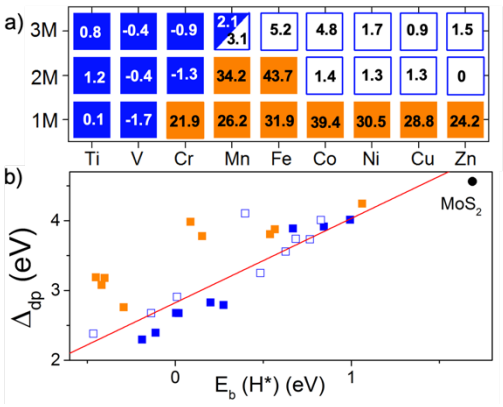

Figure 7. a) Measure of local structural distortion, $\delta d_{M\text{-}S}$ expressed as a percentage, for all dopant complexes considered. Blue (orange) boxes represent small (large) structural changes as explained in the main text. Open boxes are systems with a sulfur vacancy. b) The correlation between the interband descriptor and the hydrogen binding energy, now with structural distortion included as described in the main text. The symbol color follows that in a. The red line is the same fitted line from Figure 5b.

Our DFT calculations also show that in several of the dopant complexes, the adsorption site undergoes significant local structural distortion after H binding. So far, this structural change is not included in the discussion of descriptor and H binding in our model. The correlation shown in Figure 5b isolates the electronic structure effect captured by our model and the descriptor Δ_{dp}. To better understand the impact of local structural changes, we consider the metal-sulfur bond length change after hydrogen adsorption. Specifically, define $\delta d_{M\text{-}S} = (d_{M\text{-}S}[H^*]\text{-}d_{M\text{-}S})/\ d_{M\text{-}S}\times 100\%$ where $d_{M\text{-}S}$ is the initial distance between M-S, and $d_{M\text{-}S}[H^*]$ is the distance after H adsorption. In Figure 7a, we have listed $\delta d_{M\text{-}S}$ for all the configurations considered in this study. All the H-S bonding configurations are in Figure S8. The $\delta d_{M\text{-}S}$ can be explicitly classified into two groups: those for which $\delta d_{M\text{-}S}$<6% and $\delta d_{M\text{-}S}$>20%, represented by blue and orange blocks respectively in Figure 7a. There are clear trends. For early transition metal dopants and late transition metal dopants with V_S, the structural distortion is relatively insignificant. For late transition metal dopants for which V_S formation is not energetically favorable, the local distortions are large.

These trends carry over to the relationship between the electronic structure descriptor Δ_{dp} and the hydrogen binding energy as shown in Figure 7b. Here Δ_{dp} is computed from the relaxed defect complex structure before H adsorption. Correspondingly, the hydrogen binding energy is computed with full account of local relaxation. The resulting Δ_{dp} to E_b(H*) correlation in Figure 7b thus includes structural relaxation effects. (The complete data set can be found in Table S3.) When compared with Figure 5b, it is clear that for those dopant complexes in which there is a small structural change (blue points), the same correlation applies, albeit with somewhat more scatter. On the other hand, for dopant complexes with a large structural change (orange points), our descriptor appears to be less predictive. However, all the orange points fall above the red line. This suggests that the structural factors systematically lead the descriptor to underestimate the binding energy. Furthermore, Figure 7a shows that large structural change may be predicted based on dopant atom size and defect type (i.e. vacancy). Our current model accurately captures the electronic structure factor. Future work will be needed to refine models for the structural factors.

Conclusion

Activity of an HER catalyst can be studied through its binding energy of hydrogen atoms. In this work, we have proposed a hydrogen binding mechanism for basal plane sulfur atoms in MoS_2 based materials and validated the model using extensive DFT calculations. The H-S binding strength can be fundamentally understood to be controlled by an electronic promotion process that opens up the valence shell of the S atom. This energy cost can be tuned widely by introducing transition metal dopants which are found to form a rich array of local defect complexes, including one, two, or three dopant atoms, and a sulfur vacancy. An intrinsic descriptor, the interband energy difference between the lowest empty Mo/M *d* states and the center of occupied sulfur *p* states, captures a strong trend in the H-S binding energy. Thus, our study reveals the fundamental, electronic structure mechanism that controls the activation of basal plane S atoms in transition metal doped MoS_2 for the hydrogen evolution reaction. These insights into hydrogen binding on sulfur should extend to activation of chalcogen sites on the basal plane of transition metal dichalcogenides more generally and the design of active sites for the HER and other important electrochemical reactions.

Acknowledgements

This research is carried out at the Center for Functional Nanomaterials, which is a U.S. DOE Office of Science Facility, and used resource at the Scientific Data and Computing Center

of the Computational Science Initiative, at Brookhaven National Laboratory under Contract No. DE-SC0012704.

Keywords: Bond theory • Density functional calculations • Heterogenous catalysis • Reactivity descriptors • Transition metal dichalcogenides

[1] X. Y. Chia, A. Y. S. Eng, A. Ambrosi, S. M. Tan, M. Pumera, *Chem. Rev.* **2015**, *115*, 11941-11966.

[2] a) J. Zhang, J. J. Wu, H. Guo, W. B. Chen, J. T. Yuan, U. Martinez, G. Gupta, A. Mohite, P. M. Ajayan, J. Lou, *Adv. Mater.* **2017**, *29*, 1701955; b) C. Tsai, K. R. Chan, J. K. Norskov, F. Abild-Pedersen, *Surf. Sci.* **2015**, *640*, 133-140; c) B. Hinnemann, P. G. Moses, J. Bonde, K. P. Jorgensen, J. H. Nielsen, S. Horch, I. Chorkendorff, J. K. Norskov, *J. Am. Chem. Soc.* **2005**, *127*, 5308-5309; d) Y. F. Yu, S. Y. Huang, Y. P. Li, S. N. Steinmann, W. T. Yang, L. Y. Cao, *Nano Lett.* **2014**, *14*, 553-558; e) Y. G. Li, H. L. Wang, L. M. Xie, Y. Y. Liang, G. S. Hong, H. J. Dai, *J. Am. Chem. Soc.* **2011**, *133*, 7296-7299; f) T. F. Jaramillo, K. P. Jørgensen, J. Bonde, J. H. Nielsen, S. Horch, I. Chorkendorff, S*cience* **2007**, *317*, 100-102.

[3] X. Hong, K. R. Chan, C. Tsai, J. K. Norskov, *ACS Catal.* **2016**, *6*, 4428-4437.

[4] X. J. Chua, J. Luxa, A. Y. S. Eng, S. M. Tan, Z. Sofer, M. Pumera, *ACS Catal.* **2016**, *6*, 5724-5734.

[5] a) L. Zhang, X. Q. Ji, X. Ren, Y. J. Ma, X. F. Shi, Z. Q. Tian, A. M. Asiri, L. Chen, B. Tang, X. P. Sun, *Adv. Mater.* **2018**, *30,* 1800191; b) J. Zhang, X. Tian, M. Liu, H. Guo, J. Zhou, Q. Fang, Z. Liu, Q. Wu, J. Lou, *J. Am. Chem. Soc.* **2019**, *141*, 19269-19275.

[6] E. Skulason, G. Karlberg, J. Rossmeisl, T. Bligaard, J. P. Greeley, H. Jonsson, J. K. Norskov, *Abstr. Pap. Am. Chem. S.* **2007**, *233*.

[7] a) W. D. Williams, M. Shekhar, W. S. Lee, V. Kispersky, W. N. Delgass, F. H. Ribeiro, S. M. Kim, E. A. Stach, J. T. Miller, L. F. Allard, *J. Am. Chem. Soc.* **2010**, *132*, 14018-14020; b) N. Tian, Z. Y. Zhou, S. G. Sun, *J. Phys. Chem. C* **2008**, *112*, 19801-19817; c) M. Behrens, F. Studt, I. Kasatkin, S. Kuhl, M. Havecker, F. Abild-Pedersen, S. Zander, F. Girgsdies, P. Kurr, B. L. Kniep, M. Tovar, R. W. Fischer, J. K. Norskov, R. Schlogl, *Science* **2012**, *336*, 893-897.

[8] G. Q. Li, D. Zhang, Q. Qiao, Y. F. Yu, D. Peterson, A. Zafar, R. Kumar, S. Curtarolo, F. Hunte, S. Shannon, Y. M. Zhu, W. T. Yang, L. Y. Cao, *J. Am. Chem. Soc.* **2016**, *138*, 16632-16638.

[9] J. Kibsgaard, Z. B. Chen, B. N. Reinecke, T. F. Jaramillo, *Nat. Mater.* **2012**, *11*, 963-969.

[10] J. D. Benck, T. R. Hellstern, J. Kibsgaard, P. Chakthranont, T. F. Jaramillo, *ACS Catal.* **2014**, *4*, 3957-3971.

[11] A. A. Tedstone, D. J. Lewis, P. O'Brien, *Chem. Mater.* **2016**, *28*, 1965-1974.

[12] a) R. C. Luo, M. Luo, Z. Q. Wang, P. Liu, S. X. Song, X. D. Wang, M. W. Chen, *Nanoscale* **2019**, *11*, 7123-7128; b) J. Zhang, T. Wang, P. Liu, S. H. Liu, R. H. Dong, X. D. Zhuang, M. W. Chen, X. L. Feng, *Energ. Environ. Sci.* **2016**, *9*, 2789-2793.

[13] J. Deng, H. B. Li, J. P. Xiao, Y. C. Tu, D. H. Deng, H. X. Yang, H. F. Tian, J. Q. Li, P. J. Ren, X. H. Bao, *Energ. Environ. Sci.* **2015**, *8*, 1594-1601.

[14] a) W. Wu, C. Niu, C. Wei, Y. Jia, C. Li, Q. Xu, *Angew. Chem. Int. Ed.* **2019,** *58,* 2029-2033; b) Y. Shi, Y. Zhou, D. R. Yang, W. X. Xu, C. Wang, F. B. Wang, J. J. Xu, X. H. Xia, H. Y. Chen, *J. Am. Chem. Soc.* **2017**, *139*, 15479-15485; c) P. T. Liu, J. Y. Zhu, J. Y. Zhang, K. Tao, D. Q. Gao, P. X. Xi, *Electrochim Acta* **2018**, *260*, 24-30.

[15] Z. Luo, Y. Ouyang, H. Zhang, M. Xiao, J. Ge, Z. Jiang, J. Wang, D. Tang, X. Cao, C. Liu, *Nat. Commun.* **2018**, *9*, 2120.

[16] a) J. Deng, H. B. Li, S. H. Wang, D. Ding, M. S. Chen, C. Liu, Z. Q. Tian, K. S. Novoselov, C. Ma, D. H. Deng, X. H. Bao, *Nat. Commun.* **2017**, *8,* 14430; b) Q. Z. Xiong, Y. Wang, P. F. Liu, L. R. Zheng, G. Z. Wang, H. G. Yang, P. K. Wong, H. M. Zhang, H. J. Zhao, *Adv. Mater.* **2018**, *30,* 1801450.

[17] J. K. Norskov, T. Bligaard, A. Logadottir, J. R. Kitchin, J. G. Chen, S. Pandelov, J. K. Norskov, *J. Electrochem. Soc.* **2005**, *152*, J23-J26.

[18] J. Greeley, T. F. Jaramillo, J. Bonde, I. B. Chorkendorff, J. K. Norskov, *Nat. Mater.* **2006**, *5*, 909-913.

[19] Z. W. Seh, J. Kibsgaard, C. F. Dickens, I. B. Chorkendorff, J. K. Norskov, T. F. Jaramillo, *Science* **2017**, *355,* eaad4998.

[20] a) B. Hammer, J. K. Norskov, *Nature* **1995**, *376*, 238-240; b) B. Hammer, J. K. Norskov, *Surf. Sci.* **1995**, *343*, 211-220.

[21] a) Y. Pan, K. A. Sun, Y. Lin, X. Cao, Y. S. Cheng, S. J. Liu, L. Y. Zeng, W. C. Cheong, D. Zhao, K. L. Wu, Z. Liu, Y. Q. Liu, D. S. Wang, Q. Peng, C. Chen, Y. D. Li, *Nano Energy* **2019**, *56*, 411-419; b) Z. Y. Chen, Y. Song, J. Y. Cai, X. S. Zheng, D. D. Han, Y. S. Wu, Y. P. Zang, S. W. Niu, Y. Liu, J. F. Zhu, X. J. Liu, G. M. Wang, *Angew. Chem. Int. Ed.* **2018**, *57*, 5076-5080; c) F. Lima, J. Zhang, M. Shao, K. Sasaki, M. Vukmirovic, E. Ticianelli, R. Adzic, *J. Phys. Chem. C* **2007**, *111*, 404-410; d) N. Acerbi, S. C. E. Tsang, G. Jones, S. Golunski, P. Collier, *Angew. Chem. Int. Ed.* **2013**, *52*, 7737-7741; e) W. Y. Gou, J. Y. Li, W. Gao, Z. M. Xia, S. Zhang, Y. Y. Ma, *Chemcatchem* **2019**, *11*, 1970-1976.

[22] Y. Y. Liu, J. J. Wu, K. P. Hackenberg, J. Zhang, Y. M. Wang, Y. C. Yang, K. Keyshar, J. Gu, T. Ogitsu, R. Vajtai, J. Lou, P. M. Ajayan, B. C. Wood, B. I. Yakobson, *Nat. Energy* **2017**, *2,* 17127.

[23] L. P. Yu, Q. M. Yan, A. Ruzsinszky, *Phys. Rev. Mater.* **2019**, *3,* 092801.

[24] Y. X. Ouyang, C. Y. Ling, Q. Chen, Z. L. Wang, L. Shi, J. L. Wang, *Chem. Mater.* **2016**, *28*, 4390-4396.

[25] a) G. Kresse, J. Furthmuller, *Comp. Mater. Sci.* **1996**, *6*, 15-50; b) G. Kresse, J. Furthmuller, *Phys. Rev. B* **1996**, *54*, 11169-11186.

[26] P. E. Blochl, *Phys. Rev. B* **1994**, *50*, 17953-17979.

[27] J. Wellendorff, K. T. Lundgaard, A. Mogelhoj, V. Petzold, D. D. Landis, J. K. Norskov, T. Bligaard, K. W. Jacobsen, *Phys. Rev. B* **2012**, *85,* 235149.

[28] G. Kresse, D. Joubert, *Phys. Rev. B* **1999**, *59*, 1758-1775.

[29] K. Dolui, I. Rungger, C. Das Pemmaraju, S. Sanvito, *Phys. Rev*. B 2013, 88, 075420.

[30] M. Hakala, R. Kronberg, K. Laasonen, Sci. Rep. 2017, 7, 15243.

[31] Y. Zhou, et. al., 2020.

Supporting Information

for

A Physical Model for Understanding the Activation of MoS_2 Basal-plane Sulfur Atoms for the Hydrogen Evolution Reaction

Mingjie Liu, Mark S. Hybertsen, Qin Wu*

Center for Functional Nanomaterials, Brookhaven National Laboratory, Upton, NY, 11973

*email: qinwu@bnl.gov

Table of Contents

Computational Methods

All the DFT calculations are done with the Vienna Ab Initio Simulation Package (VASP)[1-2] using the projector augmented wave method.[3] The Bayesian error estimation exchange-correlation functionals (BEEF) with van der Waals interactions are employed.[4] A plane-wave cutoff energy of 400 eV is used together with PAW-PBE potentials where semi core *p* states are treated as valence.[5] All the calculations allow for spin-polarization. The structures are relaxed until the force is converged to < 0.01 eV/Å. The lattice parameter of MoS_2 unit cell, optimized with this functional, is 3.19 Å. A (4×4) supercell is used to model all the transition metal doped MoS_2 systems studied here, including those with S vacancies. For calculations in the initial dopant structure exploration, the Brillouin zone is sampled with a 3x3x1 Monkhorst-Pack k-point mesh. A 6×6×1 Monkhorst-Pack k-point mesh is used for the H binding energy and density of states calculations. In all calculations, the vacuum layer is set as 15 Å to eliminate periodic interaction perpendicular to the basal plane.

The sulfur vacancy (Vs) formation energy is defined as E_f(Vs)= E(Vs@nM-doped_MoS_2) + E(S) - E(nM-doped_MoS_2). The transition metal dopant is designated by M and n=1, 2 or 3 dopants are considered. The energy of a sulfur atom in the S_8 molecule is used as a reference for E(S).

The H* binding energy E_b is calculated as E_b (H*) = E(H*) - E(*) -1/2 E(H_2), where the E(H*) is the energy of H adsorbed on the surface and E(*) is the energy of substrate, and E(H_2) is the energy of an H_2 molecule in the gas phase. Defined this way, more negative E_b corresponds to stronger H* binding; positive values indicate that dissociative adsorption is unfavorable relative to the isolated gas phase molecule.

Table S1. Bond lengths of the single dopant M atom with surrounding sulfur atoms as shown in Figure 2a of the main text.

1M-doped MoS_2	l_1 (Å)	l_2 (Å)	l_3 (Å)
Ti	2.427	2.427	2.426
V	2.368	2.368	2.367
Cr	2.333	2.333	2.332
Mn	2.313	2.313	2.325
Zn	2.524	2.524	2.520

1M-doped MoS_2	l_1 (Å)	l_2 (Å)	l_3 (Å)
Fe	2.30	2.30	2.32
Co	2.27	2.27	2.56
Ni	2.23 (top)	2.23 (top)	2.46 (top)
	2.24 (bottom)	2.24 (bottom)	3.32 (bottom)
Cu	2.35 (top)	2.35 (top)	2.43 (top)
	2.39 (bottom)	2.39 (bottom)	3.17 (bottom)

Figure S1. Local structure of 1M (M=Fe, Co, Ni and Cu).

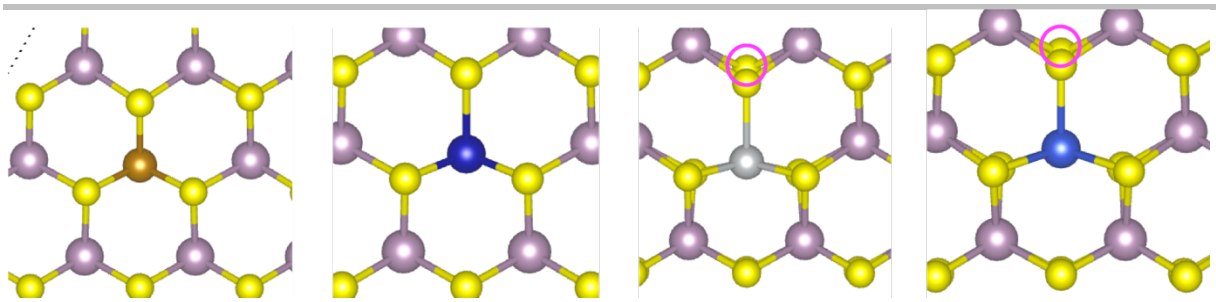

Figure S2. Three 2M configurations: $2M_S$ where two M (light blue balls) share one sulfur (yellow balls); $2M_{AC}$ where two M are in the armchair direction; and $2M_{ZZ}$ where 2M are in the zigzag direction with one Mo (light purple balls) in between.

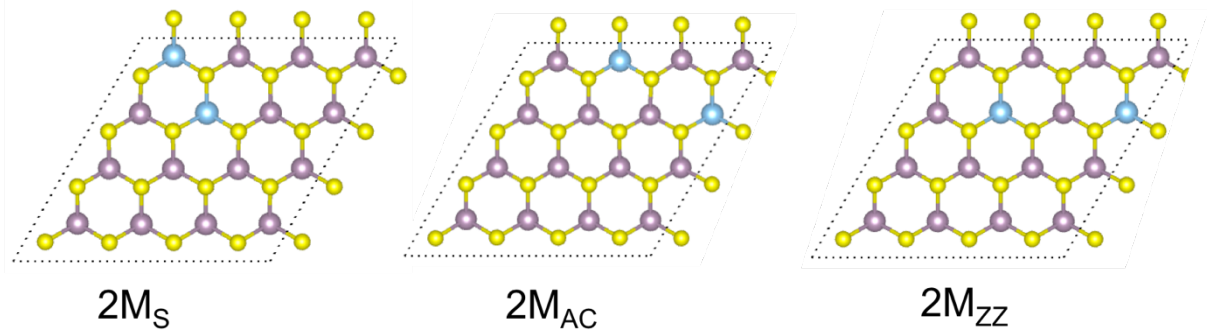

Figure S3. Optimized $2M_S$ configurations for M=Co, Ni, Cu and Zn.

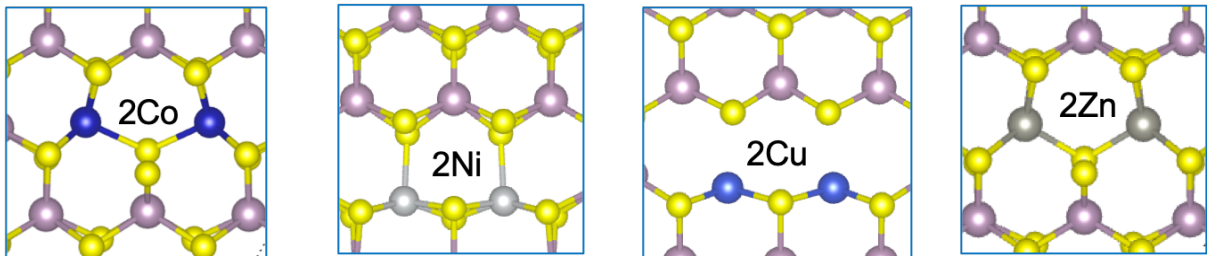

Figure S4. All eleven possible 3M configurations.

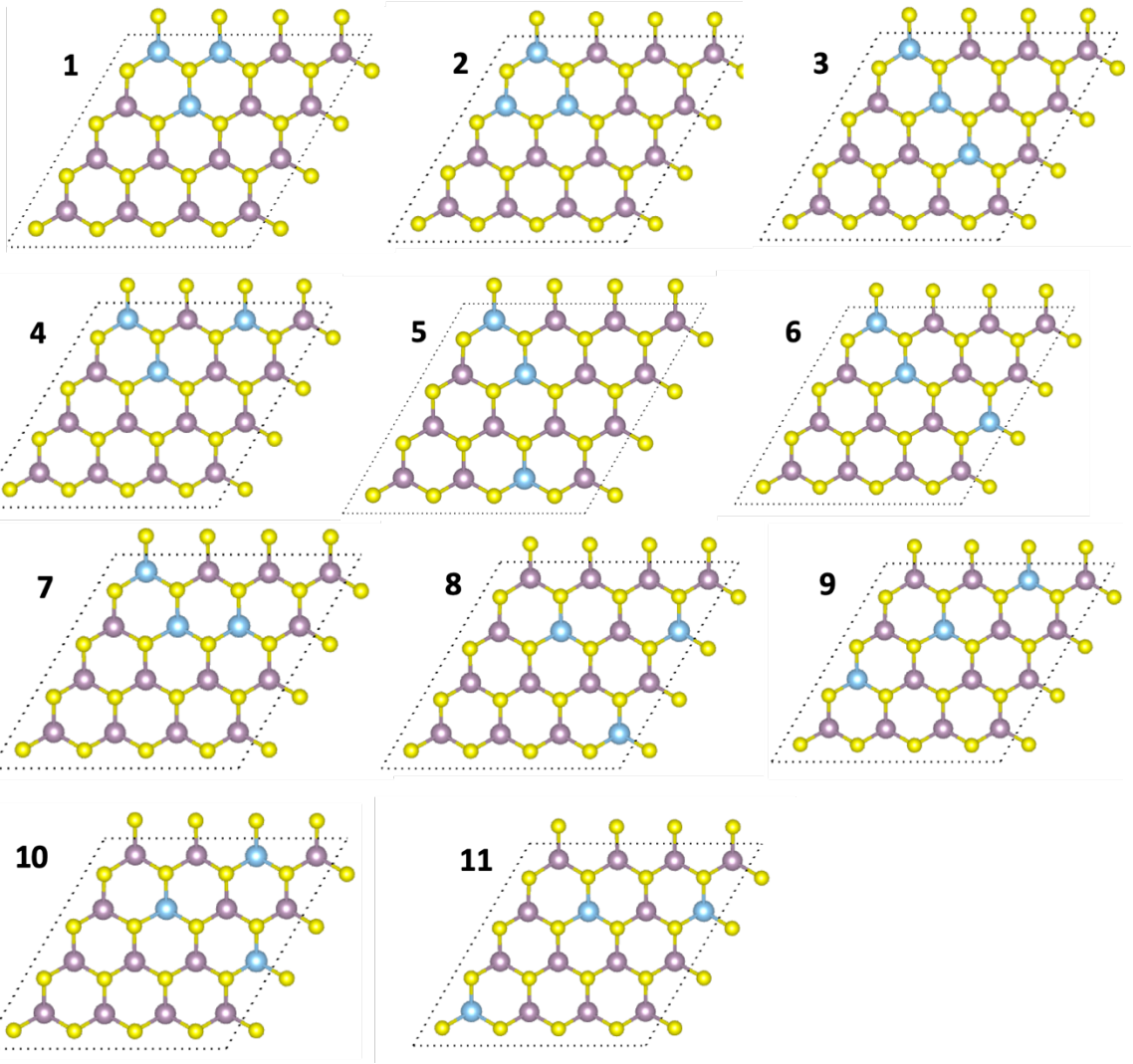
1
2
3
4
5
6
7
8
9
10
11

Figure S5. Most stable configuration for 3M (M=Co, Ni and Cu).

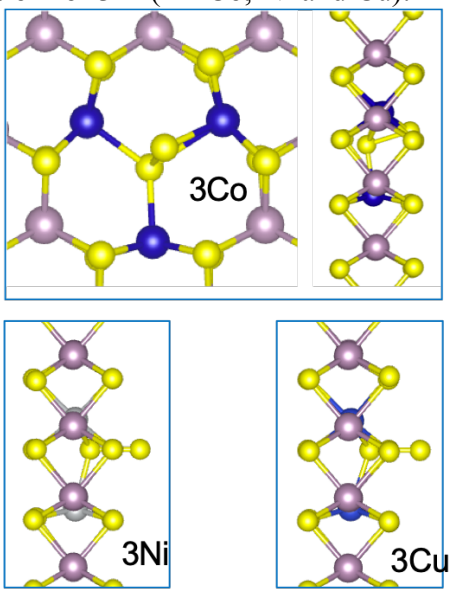

Table S2. Calculated ε_p, ε_d, the integration limit of ε_d (d_{1e}), interband energy separation Δ_{dp}, and the hydrogen binding energies. Rigid structures from the final, relaxed H-adsorption structures are used.

System	ε_p	ε_d	d_{1e}	Δ_{dp}	$E_b(H^*)$
MoS_2	-2.8993915	1.24274	1.3082	4.14213589	1.309426
1Ti	-2.7070526	0.04914	0.098	2.75619445	0.139166
2Ti	-2.229625	0.04194	0.08755	2.27156849	-0.304474
3Ti	-2.0057184	0.1029	0.141	2.10861727	-0.419224
1V	-2.8107893	0.06232	0.1424	2.873105	0.063306
2V	-2.6500591	0.04872	0.119	2.69877718	-0.136924
3V	-2.6057717	0.11158	0.1659	2.7173478	-0.145724
1Cr	-2.7025504	0.71216	0.7574	3.41471303	0.3544
2Cr	-3.2960643	0.4492	0.4983	3.74526603	0.596556
3Cr	-3.3142123	0.44461	0.4828	3.75881888	0.458016
3Mn	-3.339632	0.39478	0.5171	3.73441271	0.589866
3Mn-Vs	-2.8823924	0.08428	0.154	2.96667273	0.305376
3Fe-Vs	-3.3471417	0.11593	0.174	3.46306885	0.198036
2Co-Vs	-3.3150315	0.16711	0.2083	3.48214163	0.413886
3Co-Vs	-2.9366303	0.14415	0.195	3.08078458	-0.402244
2Ni-Vs	-3.2011419	0.0189	0.0767	3.2200419	0.423656
3Ni-Vs	-2.3385398	0.22811	0.26	2.56664545	-0.176124
2Cu-Vs	-3.0997737	0.0397	0.0922	3.13947371	0.349076
3Cu-Vs	-2.1922143	0.0265	0.081	2.21871432	-0.532634
2Zn-Vs	-3.1474784	0.05029	0.0878	3.19776488	0.411266
3Zn-Vs	-2.2755213	0.17173	0.2078	2.44725331	-0.269504
1Mn	-2.4762153	0.22583	0.2794	2.70204999	0.098276
1Fe	-2.4593659	0.11054	0.178	2.56990216	-0.268454
1Co	-2.1893566	0.05678	0.1	2.24613573	-0.638144
1Ni	-1.9337637	0.07704	0.1127	2.01080775	-0.694044

1Cu	-1.9292747	0.06873	0.0996	1.99800014	-0.627014
1Zn	-2.0669574	0.04849	0.0824	2.11544546	-0.523414
2Mn	-1.7059475	0.0673	0.11	1.77325179	-0.843144
2Fe	-1.6783617	0.18476	0.239	1.86312432	-0.874334

Figure S6. Relationship between E_b(H*) and ε_p. Black dots are systems with significant band gaps.

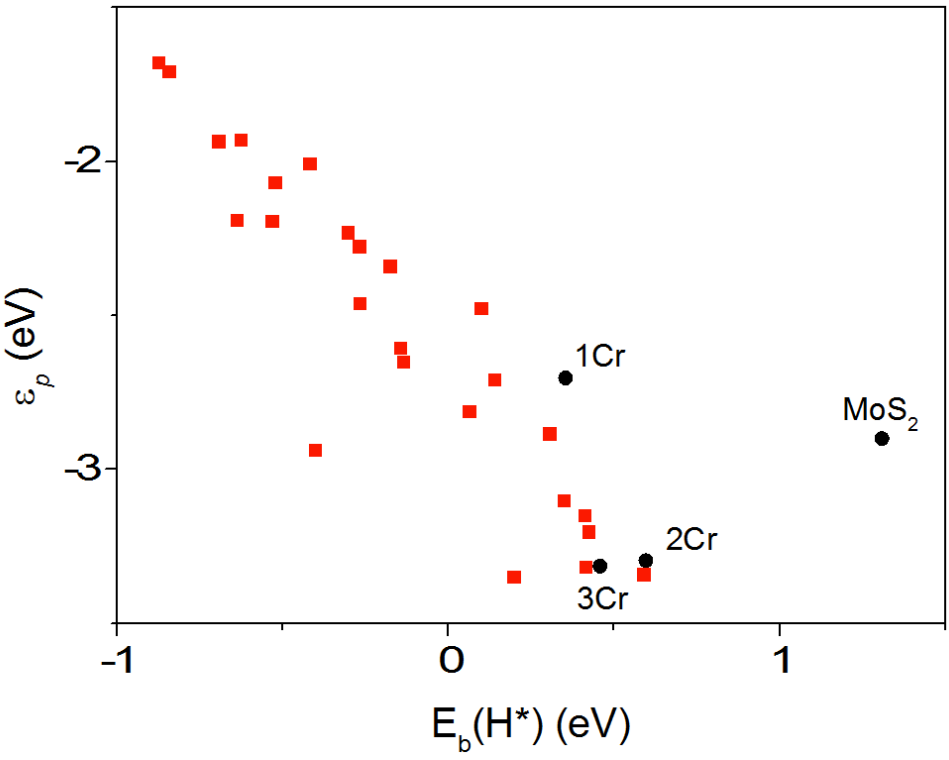

Figure S7. Relationship between $E_b(H^*)$ and Bader charge of the active S atom. Purple dots denote systems considered by Deng et al. (Reference 27 in the main text). The dashed line in is $E_b(H^*)$ = -0.24 eV, corresponding to the $\Delta G(H^*)$ = 0 in the same reference. Charge densities are calculated on a 384x384x480 grid.

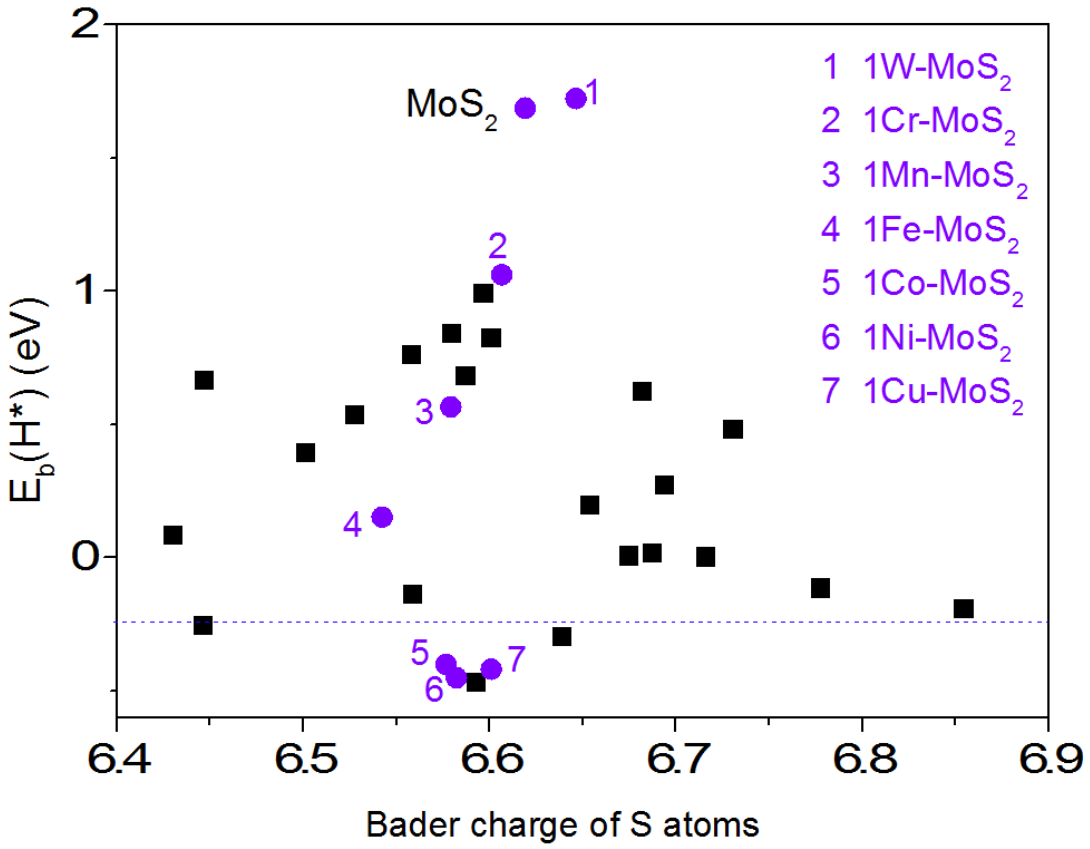

Figure S8. Hydrogen-sulfur binding configuration for all studied systems.

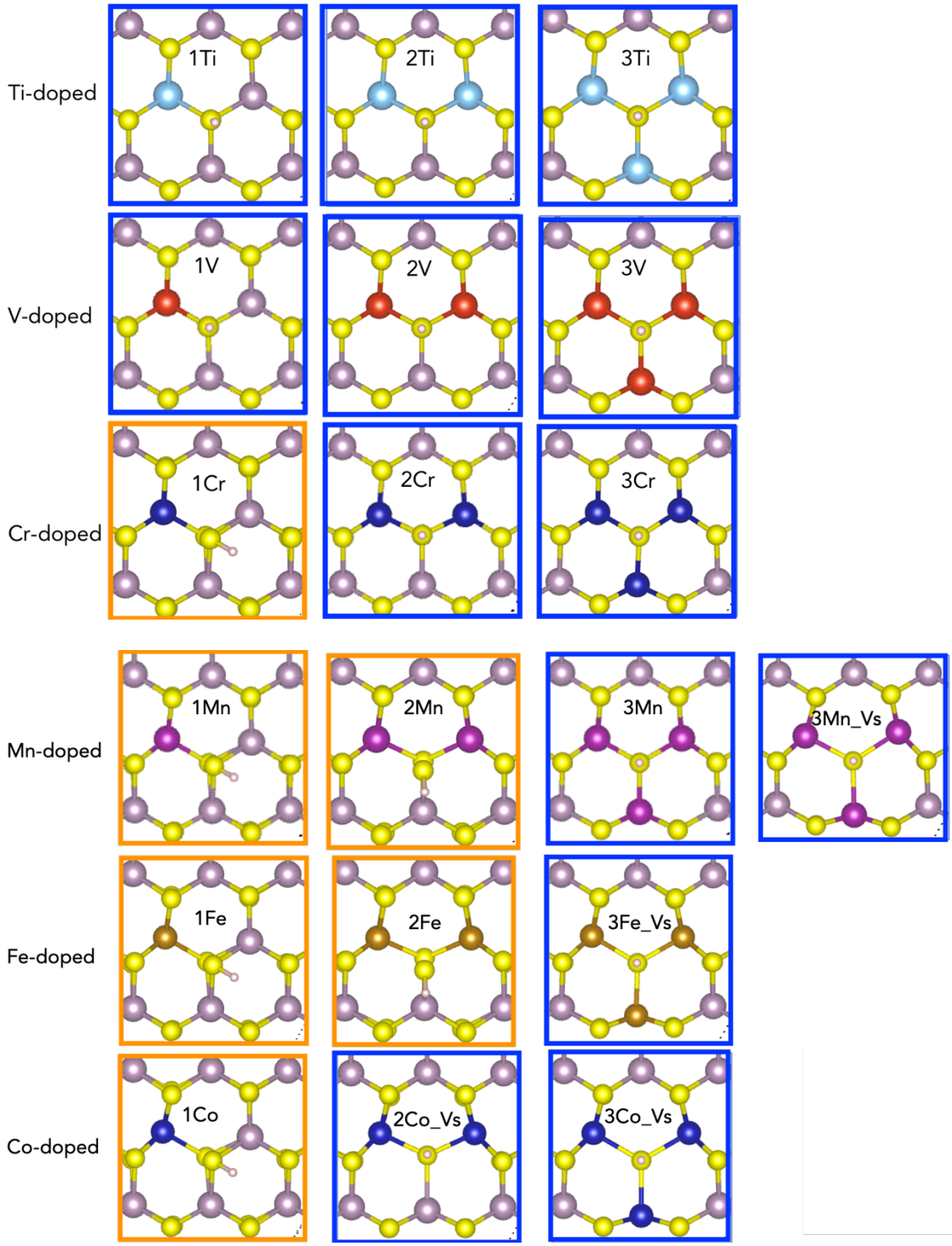

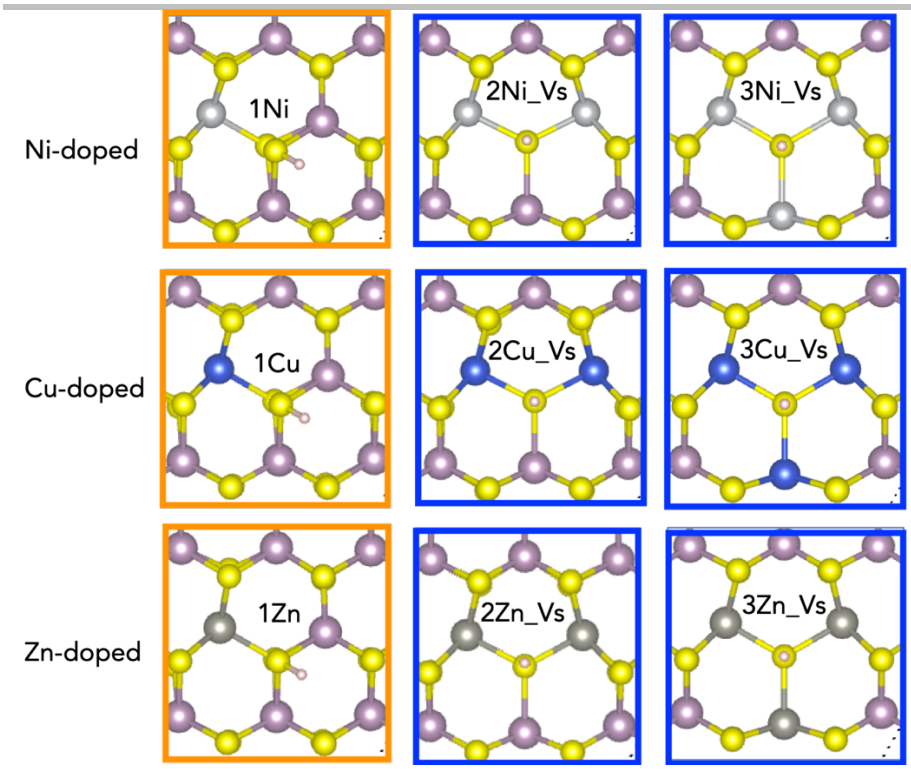
Ni-doped
1Ni
2Ni_Vs
3Ni_Vs
Cu-doped
1Cu
2Cu_Vs
3Cu_Vs
Zn-doped
1Zn
2Zn_Vs
3Zn_Vs

Table S3. Calculated ε_p, ε_d, the integration limit of ε_d (d_{1e}), interband energy separation Δ_{dp}, and the hydrogen binding energies. Here the relaxed structure before hydrogen adsorption is used, and the hydrogen binding energy has full account of relaxation.

System	ε_p	ε_d	d_{1e}	Δ_{dp}	E_b(H*)
MoS_2	-3.304377	1.25787826	1.3273	4.56225565	1.688106
1Ti	-2.747181	0.04273743	0.93	2.78991885	0.274886
2Ti	-2.355788	0.03881592	0.0655	2.39460385	-0.111594
3Ti	-2.165402	0.1307738	0.1613	2.29617602	-0.188024
1V	-2.762203	0.06551125	0.1504	2.82771451	0.200346
2V	-2.626123	0.04755285	0.12	2.67367577	0.019586
3V	-2.559217	0.11642233	0.1616	2.67563906	0.005406
1Cr	-3.274815	0.96904979	1.0099	4.24386494	1.061976
2Cr	-3.259043	0.75304893	0.7903	4.01209213	0.993316
3Cr	-3.203719	0.71233538	0.7458	3.9160544	0.844686
3Mn	-3.505537	0.38104377	0.4865	3.88658027	0.668566
3Mn_Vs	-3.174336	0.07385404	0.2077	3.24819049	0.483766
3Fe_Vs	-3.976215	0.12872765	0.189	4.10494256	0.397316
2Co_Vs	-3.863204	0.1445021	0.2113	4.00770565	0.827426
3Co_Vs	-3.639318	0.03662774	0.12	3.675946	-0.251984
2Ni_Vs	-3.681971	0.0514	0.0605	3.7333709	0.765356
3Ni_Vs	-2.449433	0.22568952	0.2636	2.67512257	-0.136304
2Cu_Vs	-3.691698	0.0484	0.1017	3.74009844	0.684946
3Cu_Vs	-2.348453	0.0315	0.1	2.37995298	-0.465094
2Zn_Vs	-3.524369	0.03171496	0.08	3.55608443	0.627336
3Zn_Vs	-2.707806	0.20002557	0.234	2.90783196	0.010086
1Mn	-3.805745	0.06994366	0.1074	3.87568855	0.566196
1Fe	-3.646866	0.13067455	0.2097	3.77754006	0.152916
1Co	-3.01931	0.15829479	0.207	3.17760439	-0.400714
1Ni	-3.097258	0.09074048	0.1574	3.18799844	-0.450484
1Cu	-3.015908	0.0611	0.0993	3.0770083	-0.418124
1Zn	-2.710408	0.04863322	0.1017	2.75904146	-0.292904
2Mn	-3.740842	0.06544782	0.11	3.80628937	0.539196
2Fe	-3.875554	0.1080545	0.1683	3.9836087	0.086816

References:

1. Kresse, G.; Furthmuller, J., Efficiency of ab-initio total energy calculations for metals and semiconductors using a plane-wave basis set. *Comp Mater Sci* **1996,** *6* (1), 15-50.
2. Kresse, G.; Furthmuller, J., Efficient iterative schemes for ab initio total-energy calculations using a plane-wave basis set. *Phys Rev B* **1996,** *54* (16), 11169-11186.
3. Blochl, P. E., Projector Augmented-Wave Method. *Phys Rev B* **1994,** *50* (24), 17953-17979.
4. Wellendorff, J.; Lundgaard, K. T.; Mogelhoj, A.; Petzold, V.; Landis, D. D.; Norskov, J. K.; Bligaard, T.; Jacobsen, K. W., Density functionals for surface science: Exchange-correlation model development with Bayesian error estimation. *Phys Rev B* **2012,** *85* (23).
5. Kresse, G.; Joubert, D., From ultrasoft pseudopotentials to the projector augmented-wave method. *Phys Rev B* **1999,** *59* (3), 1758-1775.